

This is the accepted manuscript made available via CHORUS. The article has been published as:

One-dimensional carbon nanostructures for terahertz electron-beam radiation

Khwanchai Tantiwanichapan, Anna K. Swan, and Roberto Paiella

Phys. Rev. B **93**, 235416 — Published 10 June 2016

DOI: [10.1103/PhysRevB.93.235416](https://doi.org/10.1103/PhysRevB.93.235416)

One-dimensional carbon nanostructures for terahertz electron-beam radiation

Khwanchai Tantiwanichapan¹, Anna K. Swan^{1,2}, and Roberto Paiella^{1,a}

¹ Department of Electrical and Computer Engineering and Photonics Center,
Boston University, 8 Saint Mary's Street, Boston, MA 02215

² Department of Physics, Boston University, 590 Commonwealth Avenue, Boston, MA 02215

Abstract: One-dimensional carbon nanostructures such as nanotubes and nanoribbons can feature near-ballistic electronic transport over micron-scale distances even at room temperature. As a result, these materials provide a uniquely suited solid-state platform for radiation mechanisms that so far have been the exclusive domain of electron beams in vacuum. Here we consider the generation of terahertz light based on two such mechanisms, namely the emission of cyclotron-like radiation in a sinusoidally corrugated nanowire (where periodic angular motion is produced by the mechanical corrugation rather than an externally applied magnetic field), and the Smith-Purcell effect in a rectilinear nanowire over a dielectric grating. In both cases, the radiation properties of the individual charge carriers are investigated via full-wave electrodynamic simulations, including dephasing effects caused by carrier collisions. The overall light output is then computed with a standard model of charge transport for two particularly suitable types of carbon nanostructures, i.e., zigzag graphene nanoribbons and

^a Electronic mail: rpaiella@bu.edu

armchair single-wall nanotubes. Relatively sharp emission peaks at geometrically tunable THz frequencies are obtained in each case. The corresponding output powers are experimentally accessible even with individual nanowires, and can be scaled to technologically significant levels using array configurations. These radiation mechanisms therefore represent a promising new paradigm for light emission in condensed matter, which may find important applications in nanoelectronics and THz photonics.

PACS numbers: 41.60.-m, 78.67.Ch, 73.23.Ad

I. INTRODUCTION

Carbon nanostructures including graphene and nanotubes represent a promising materials platform for future device applications in nanoelectronics and photonics. Of particular interest for such applications are the large carrier mobilities of these materials, which have enabled the observation of ballistic electronic transport over micron-scale distances even at room temperature. Specific examples of such ballistic samples reported to date include single- and multi-wall carbon nanotubes [1-4], suspended graphene sheets [5, 6], graphene/boron-nitride heterostructures [7, 8], and epitaxial graphene nanoribbons [9]. Because of their exceptionally long mean free paths, a distinctive analogy can be drawn between the electron (and hole) gases in these nanomaterials and electron beams in vacuum-based systems, so that novel applications inspired by traditional vacuum-tube devices may be envisioned. In the present work, we investigate numerically the use of one-dimensional (1D) carbon nanostructures for the generation of terahertz light based on two related electron-beam radiation mechanisms: (I) the emission of cyclotron-like radiation in the presence of mechanical corrugation (as opposed to an externally

applied magnetic field), and (II) the Smith-Purcell effect (i.e., radiation by charges in uniform rectilinear motion near a grating [10]). Similar electron-beam radiation mechanisms already form the basis of well-established vacuum-tube devices such as free-electron lasers (FELs) [11] and microwave magnetrons and orotrons [12]. At the same time, they represent a radically new paradigm for light emission in condensed matter, with very limited prior work (either experimental [13] or theoretical [14-16]) involving traditional semiconductors.

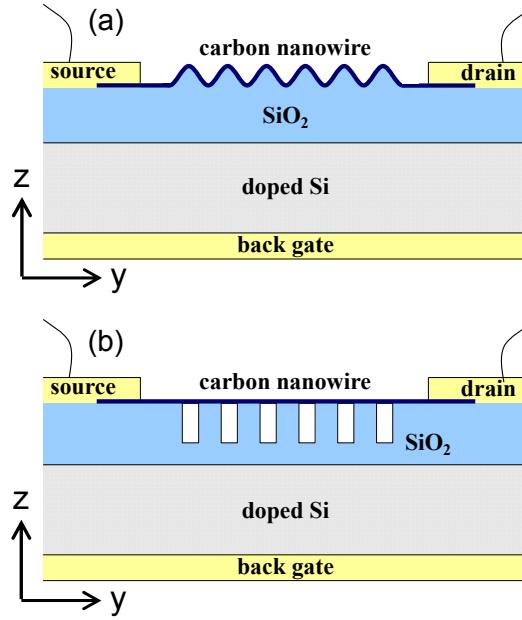


FIG. 1: Schematic cross-sectional view of representative device structures for the demonstration of THz electron-beam radiation in 1D carbon nanostructures. (a) Corrugated carbon nanowire for the generation of cyclotron-like THz radiation. (b) Carbon nanowire in the near-field vicinity of a grating for the generation of THz Smith-Purcell radiation.

The basic sample geometries under study are illustrated schematically in Fig. 1. In Fig. 1(a), a 1D conductor (such as a carbon nanotube or graphene nanoribbon) is corrugated mechanically to produce a sinusoidal trajectory. In practice, this geometry could be realized through the direct growth or conformal transfer of the conducting wire on a substrate surface patterned in the shape of a sinusoidal grating. Because of the conductor 1D nature, in the

presence of a bias voltage the injected electron (or hole) trajectories are confined to the sinusoidal path defined by the corrugation. As a result, radiation is produced by these carriers due to their periodic angular motion. This mechanism is analogous to cyclotron radiation in FELs, except that the angular motion is obtained via geometrical constraints rather than through the application of an external magnetic field (e.g., with a periodic array of alternating magnets as in typical FEL undulators).

In Fig. 1(b), we consider a rectilinear conducting wire in the immediate vicinity of a periodic dielectric grating, which could be patterned in the supporting substrate (as in the figure) or fabricated directly above the wire. In this case, radiation can still be emitted by the charge carriers in the 1D conductor as they pass near the grating under uniform rectilinear motion, via the Smith-Purcell effect. This radiation mechanism was initially discovered through the observation of visible light emission from a high-energy electron beam traveling near a metallic grating in vacuum [10]. In a simple picture, the emitted radiation can be attributed to the periodic angular motion of the polarization charges that are induced under the grating surface by the moving charges in the electron beam. More precisely, the underlying physical mechanism can be explained in terms of the evanescent electromagnetic fields that are created by the actual moving charges and then diffractively scattered into radiation by the grating [17]. The use of the Smith-Purcell effect for the generation of microwaves in vacuum-based devices (orotrons) is already well established [12]. Its observation in condensed matter has also been reported, with a high-mobility GaAs/AlGaAs heterojunction, but only at cryogenic temperatures and with extremely broad and weak output spectra [13].

The ability of carbon nanostructures to provide micron-scale ballistic transport is critically important for both radiation mechanisms. In a previous study [14], a related device

geometry [i.e., a semiconductor two-dimensional electron gas (2DEG) adjacent to a grating] was investigated theoretically in the regime of classical drift transport, as described with a hydrodynamic model. In this regime, the carriers flowing through the sample can become strongly coupled to plasma oscillations, and the radiation output was found to be dominated by the diffractive scattering of these collective excitations by the grating [18]. THz emission from grating-coupled 2D plasmons has in fact been reported in several experimental studies with semiconductor 2DEGs [19-22]. In contrast, in the (quasi)ballistic conductors under study the injected carriers can flow through the entire sample (or a significant fraction of its length covering several grating periods) at constant velocity without any collisions involving plasma oscillations or any other scattering mechanism. Radiation can then be produced through the interaction of the individual carriers with the grating, in closer analogy with the original Smith-Purcell experiment.

For both radiation mechanisms of Fig. 1, the emission frequency is on the order of v/Λ (as shown in detail below), where v is the Fermi velocity and Λ the period of either the sinusoidal trajectory or the nearby grating. In metallic carbon nanostructures, the low-energy electrons and holes generally feature a relatively large Fermi velocity near $v_F \approx 1 \times 10^8$ cm/s. As a result, cyclotron-like and Smith-Purcell radiation frequencies spanning the entire THz spectrum can be obtained with periods of a few hundred nanometers. Importantly, such values of Λ are smaller than the maximum mean free paths for room-temperature ballistic transport achievable with the devices under study, but still large enough for their practical implementation. Therefore, these devices can provide a promising new approach to address a key technology gap of modern-day optoelectronics, namely the lack of practical solid-state THz sources capable of room-temperature operation [23]. The use of carbon nanomaterials for THz science and

technology has already become the subject of increasing interest [24-26], motivated by their unique electronic properties. In the area of THz sources, several theoretical proposals involving graphene [27-33] or carbon nanotubes [34-39] have been presented, based on several mechanisms including interband electronic transitions, tunable plasmonic excitations, or real-space charge oscillations. The experimental demonstrations of THz amplification and emission in optically pumped samples have also already been reported [40-44].

In recent work, we have investigated numerically the feasibility of THz electron-beam radiation from the 2DEG in corrugated [45] or grating-coupled [46] graphene sheets. In both cases, promising results were obtained in terms of radiated optical power and tunability of the emission frequencies. Here we consider instead two specific types of 1D carbon nanostructures, namely zigzag graphene nanoribbons (ZZ-GNRs) and metallic armchair single-wall nanotubes (AC-SWNTs). The use of 1D conductors for electron-beam radiation is intuitively compelling in light of the aforementioned analogy with vacuum-tube devices, where all electrons can be made to travel roughly along the same direction. In contrast, in a condensed-matter 2DEG the carrier distribution in reciprocal space is such that, even in the presence of a bias voltage, there are carriers traveling along all possible directions on the 2DEG plane. Such carriers radiate at different frequencies and with different efficiency depending on their direction of motion relative to the corrugation or grating. Therefore, 1D conductors can be expected to provide narrower and stronger emission peaks, as confirmed by our simulation results presented below. In addition, both zigzag-like GNRs [9] and metallic SWNTs [3, 4] have already been shown to exhibit robust ballistic transport over distances longer than 1 μm even at room temperature. Therefore, they both represent a particularly suitable system to investigate THz electron-beam radiation in condensed matter, with significant promise for future technological impact.

The remainder of the article is organized as follows. The electronic band structure and state-of-the-art transport properties of the 1D nanomaterials under study are briefly reviewed in the next section. In Section III we describe the simulation methods used to compute the electron-beam radiation output, which involve full-wave electrodynamic calculations based on the finite difference time domain (FDTD) approach combined with a standard model of charge transport in (quasi)ballistic conductors. The important effect of carrier collisions is also included in these FDTD simulations, by adjusting the length over which the motion of each electron (and therefore its radiation output) is coherent. In Section IV we present the calculated emission spectra for both radiation mechanisms (cyclotron-like and Smith-Purcell) in both types of nanostructure (ZZ-GNRs and AC-SWNTs), and discuss how the output power and emission frequency depend on the corrugation or grating period Λ . The main conclusions of this study are finally summarized in Section V.

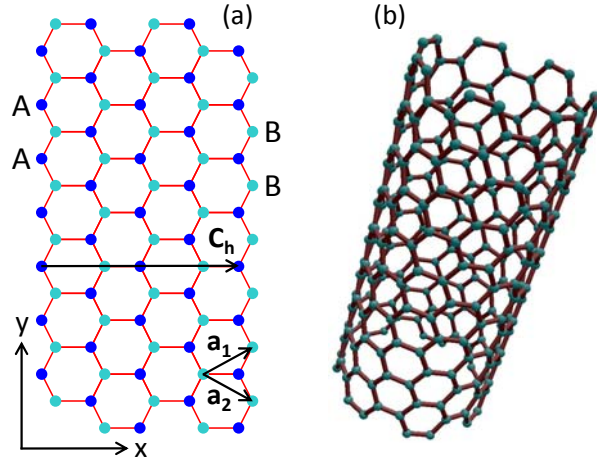


FIG. 2: Crystal structure of the 1D carbon nanowires under study: (a) ZZ-GNR; (b) AC-SWNT. In (a), \mathbf{a}_1 and \mathbf{a}_2 are the basis vectors of the crystal lattice, \mathbf{C}_h is the chiral vector, and the letters A and B indicate representative carbon atoms belonging to the two sub-lattices.

II. 1D CARBON NANOSTRUCTURES

A. Graphene nanoribbons

The crystal structure of a ZZ-GNR (oriented along the y direction) is shown schematically in Fig. 2(a). As in all sp^2 -hybridized carbon allotropes, the underlying lattice is triangular with two carbon atoms per unit cell, denoted A and B. In zigzag nanoribbons, all atoms on each edge parallel to the ribbon axis belong to the same sublattice (A on one edge, B on the other). The opposite extreme is that of armchair edges, which consist of an equal number of alternating A and B atoms. This distinction is important, because the edge shape has a profound impact on the nanoribbon electronic band structure [47]. In particular, ZZ-GNRs support localized edge states near the Fermi energy. In contrast, in armchair nanoribbons edge states are absent, and an energy bandgap can be found depending on the ribbon width. In practice, the edges of typical nanoribbons contain both zigzag and armchair sections, and the electronic properties tend to be dominated by the zigzag sites [48]. Therefore, our present focus on ZZ-GNRs is quite general in terms of applicability to practical samples. Furthermore, the main channel for ballistic transport measured in graphene nanoribbons so far is actually associated with the low-energy subbands involving edge states [9], which are characteristic of zigzag-like samples only.

In general, the energy band diagram of any graphene-derived nanostructure can be computed from that of graphene through the application of suitable boundary conditions. In graphene, the conduction and valence bands are well described by the following analytical expression based on a simple tight-binding model [48],

$$E_{\pm}(\mathbf{k}) = \pm t \sqrt{1 + 4 \cos\left(\frac{\sqrt{3}k_x a}{2}\right) \cos\left(\frac{k_y a}{2}\right) + 4 \cos^2\left(\frac{k_y a}{2}\right)}, \quad (1)$$

where a is the length of the lattice basis vectors \mathbf{a}_1 and \mathbf{a}_2 , and t is the nearest-neighbor hopping parameter. According to eq. (1), the bandgap energy $E_+ - E_-$ is zero at two distinct high-

symmetry points within the first Brillouin zone, labeled K and K'. In the vicinity of these points, both bands have conical dispersion $E_{\pm} \approx \pm \hbar v_F k$, where the wavevector k is measured from K or K' and $v_F = (\sqrt{3}ta)/(2\hbar)$ is the Fermi velocity. This behavior is similar to that of ultra-relativistic particles described by the massless Dirac equation, albeit at smaller speeds. A two-dimensional analogue of the massless Dirac equation can in fact be derived from eq. (1) using the $\mathbf{k} \cdot \mathbf{p}$ approximation. In this formulation, the states near the K point are described by a two-component energy eigenvector $\Psi_K = [\Psi_{KA}, \Psi_{KB}]^T$, where Ψ_{KA} and Ψ_{KB} are the electronic envelope functions over sublattices A and B, respectively. Then, the appropriate boundary condition for a zigzag-like edge that mostly contains atoms of one sublattice (e.g., A) is that the envelope functions associated with the other sublattice (Ψ_{KB}) must vanish everywhere along the edge [49]. Application of this condition to a ZZ-GNR of width W leads to the following dispersion relation

$$\tanh(\alpha W) = \pm \alpha/k, \quad (2)$$

where k indicates the electronic wavevector along the ribbon axis, and the parameter α is related to the energy eigenvalues E according to $E = \pm \hbar v_F \sqrt{k^2 - \alpha^2}$. The nanoribbon subbands are finally computed by solving eq. (2) for E as a function of k .

Representative results are shown in Fig. 3 for a ZZ-GNR of 40-nm width. Of particular interest here are the lowest-energy conduction and valence subbands, which exhibit a nearly flat dispersion for k between $K_y = 2\pi/3a$ and $K'_y = 4\pi/3a$ (the y components of the wavevector at K and K', respectively). Vice versa, for $k < K_y$ or $> K'_y$, the slope of both bands rapidly increases to the graphene limit of $dE/dk = \pm \hbar v_F$. These subbands contain the aforementioned localized states confined near the edges of the nanoribbon, as can be verified by computing the corresponding envelope functions. In contrast, for all states in the remaining subbands, the

wavefunctions are delocalized across the entire width of the nanoribbon. More detailed band structure calculations also show that electron-electron interactions can lift the degeneracy of the partially flat subbands, thereby opening a bandgap even in ZZ-GNRs [49, 50]. However, whether these modifications are included or not in our analysis, the Fermi level can still be pushed to the high-slope portion of the lowest-energy conduction (or valence) subband at similar carrier densities. The resulting radiation spectra are then going to be essentially the same, since they are mostly determined by the carriers near the Fermi level.

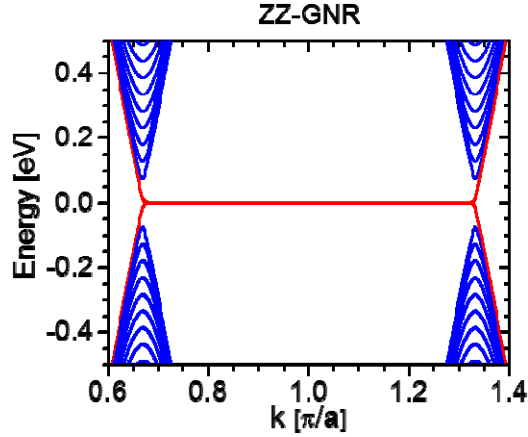


FIG. 3: Electronic band structure of a ZZ-GNR with 40-nm width. The wavevector k is measured along the axis of the nanoribbon, relative to the center of the graphene first Brillouin zone.

The possibility of ballistic transport in graphene nanoribbons even in the presence of disorder has been investigated theoretically in Ref. 51. The key conclusion of this study is that the lowest-energy conduction and valence subbands involving edge states can provide a perfectly conducting channel, as long as impurity scattering is sufficiently long range that it cannot promote intervalley transitions (i.e., from states near Γ to states near K , and vice versa). The underlying physics is related to the violation of pseudo time-reversal symmetry associated with the different number of forward and backward traveling modes within each valley. Experimentally, room-temperature ballistic transport associated with these conducting channels

has been measured in ~ 40 -nm-wide nanoribbons, over distances as long as $16\ \mu\text{m}$ [9]. In contrast, transport in the higher-energy subbands of the same samples was found to be diffusive, with much shorter mean free paths of about $200\ \text{nm}$. The nanoribbons used in these measurements were synthesized via epitaxial growth on SiC, a technique that can be scaled to high-density arrays over large device areas.

B. Carbon nanotubes

The other type of 1D nanostructure considered in this work, AC-SWNTs, is illustrated schematically in Fig. 2(b). These nanotubes can be conceptually visualized as ZZ-GNRs rolled up about their long axes, so that both ends of the resulting nanocylinders feature armchair edges. As shown in Fig. 2(a), the chiral vector of AC-SWNTs (i.e., the vector running across the unrolled nanotube perpendicular to its axis) is $\mathbf{C}_h = n(\mathbf{a}_1 + \mathbf{a}_2) = \sqrt{3}na\hat{\mathbf{x}}$, where n is an integer related to the tube circumference $C = \sqrt{3}na$. In general, the electronic band structure of carbon nanotubes can be obtained from that of graphene by imposing periodic boundary conditions with periodicity C along the direction of the chiral vector, i.e., by requiring that the wavevector component in the direction of \mathbf{C}_h is quantized in integral multiples of $2\pi/C$ [52]. For AC-SWNTs, this condition simply becomes

$$k_x = \frac{2s\pi}{\sqrt{3}na}, \quad (3)$$

for any integer s between 1 and $2n$.

Figure 4 shows the electronic band structure of an AC-SWNT with $n = 15$ (corresponding to a typical tube diameter C/π of $2\ \text{nm}$), computed by substituting eq. (3) into eq. (1). As illustrated by this plot, AC-SWNTs are metallic, which follows from the fact that the crystal wavevectors of the high-symmetry points K and K' (where the graphene bandgap is zero) satisfy the boundary condition of eq. (3) for $s = n$. As a result, the conical shape with slope $\hbar v_F$

and the zero-energy crossing of the graphene conduction and valence bands near K and K' are preserved in the $s = n$ subbands of AC-SWNTs near Γ and Γ' . This arrangement is particularly favorable for the radiation mechanisms under study, because all electrons and holes in the main conducting channels (the $s = n$ subbands) travel at the same, relatively high velocity v_F , and therefore can radiate at the same frequency with relatively high output power. In passing we note that approximately one third of all possible types of SWNTs (depending on their chiral vector \mathbf{C}_h) can be expected to be metallic based on similar arguments. Therefore, the calculation results presented below may also be extended to these other types of nanotubes, although in many instances (but not in AC-SWNTs) curvature effects lead to the opening of a small bandgap [52].

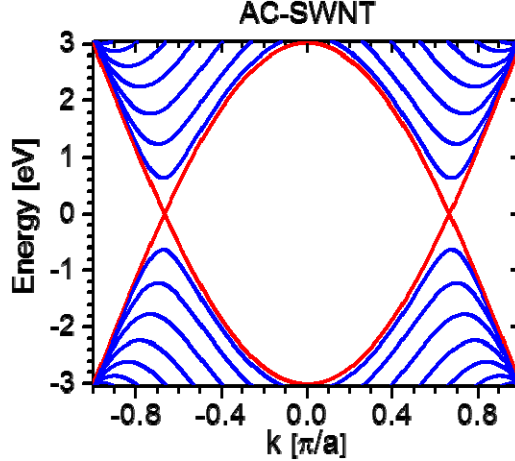


FIG. 4: Electronic band structure of an AC-SWNT with 2-nm diameter. The wavevector k is measured along the axis of the nanotube, relative to the center of the graphene first Brillouin zone.

The electronic transport properties of metallic SWNTs have been widely investigated over the past several years, including the theoretical prediction [53] and experimental observation of (quasi)ballistic conduction [2-4]. At room temperature, the electronic mean free path l_m of high-quality samples is limited by electron-phonon scattering and its specific value depends on the applied voltage. At low bias (less than about 0.2 V), no carrier has sufficient

energy to emit an optical phonon, and the mobility is limited by a relatively weak acoustic-phonon scattering mechanism, leading to large mean free paths exceeding 1 micron [3]. At higher voltages, the emission of optical phonons becomes allowed, and l_m is correspondingly decreased by an order or magnitude. Finally, at low temperatures and low bias, mean free paths as long as $\sim 8 \mu\text{m}$ have been measured, only limited by impurity scattering [4]. In general, the electron-beam radiation mechanisms under study require ballistic transport over at least a few periods Λ of the sinusoidal trajectory or nearby grating, and THz radiation frequencies are obtained with periods of a few 100 nm. Therefore, metallic SWNTs also appear to be suitable for these mechanisms, even at room temperature, as long as the applied voltage is kept sufficiently small.

III. SIMULATION METHODS

In order to investigate the radiation properties of the nanostructures of Fig. 1, we first consider an arbitrary individual electron in these 1D conductors and compute its light output using the FDTD method. In these calculations, the moving electron is modeled with an equivalent distribution of oscillating dipoles, so that the built-in dipole radiation sources of the FDTD simulation engine [54] can be employed. The polarization density of the equivalent dipole distribution $\mathbf{P}(\mathbf{r}, t)$ is derived from the current density carried by the electron $\mathbf{J}(\mathbf{r}, t)$ based on the general relationship $\mathbf{J}(\mathbf{r}, t) = \partial \mathbf{P}(\mathbf{r}, t) / \partial t$ [i.e., $\mathbf{J}(\mathbf{r}, \omega) = -i\omega \mathbf{P}(\mathbf{r}, \omega)$ in the frequency domain] [55]. Here $\mathbf{J}(\mathbf{r}, t) = -q \dot{\mathbf{r}}_e(t) \delta(\mathbf{r} - \mathbf{r}_e(t))$, where $-q$ is the electron charge and the electron trajectory $\mathbf{r}_e(t)$ depends on the specific device geometry. In the corrugated wire of Fig. 1(a) (where the corrugation is along the y direction),

$$\mathbf{r}_e(t) = \hat{\mathbf{y}}y_e(t) + \hat{\mathbf{z}}A\sin(2\pi y_e(t)/\Lambda), \quad (4)$$

where A and Λ are the corrugation amplitude and period, respectively. The electron instantaneous position along the y direction, $y_e(t)$, can be calculated numerically as a function of time by combining eq. (4) with

$$|\dot{\mathbf{r}}_e(t)| = v_k = dE/d(\hbar k), \quad (5)$$

where k is the electronic wavevector along the axis of the wire and $E(k)$ is the electron energy (computed as a function of k as described in the previous section). Equation (5) simply expresses the condition that, if the electron occupies the Bloch state of wavevector k , its speed is equal to v_k . To determine the equivalent polarization density, we Fourier transform $\mathbf{J}(\mathbf{r}, t)$ and divide the result by $-i\omega$, leading to the following expression:

$$\mathbf{P}(\mathbf{r}, \omega) = \frac{q}{i\omega} \left[\hat{\mathbf{y}} + \hat{\mathbf{z}} \frac{2\pi A}{\Lambda} \cos(2\pi y/\Lambda) \right] \delta(x) \delta(z - A \sin(2\pi y/\Lambda)) e^{i\omega t(y)}, \quad (6)$$

where $t(y)$ is the time instant when the electron position along the corrugation satisfies $y_e(t) = y$. For the Smith-Purcell geometry of Fig. 1(b), eqs. (4)-(6) still apply with the corrugation amplitude A set equal to zero, in which case the electron position along the y direction (i.e., perpendicular to the grating lines) simply becomes $y_e(t) = v_k t$.

Equation (6) describes a continuous distribution of electric dipoles linearly positioned along the electron trajectory, having position-dependent magnitude, phase and direction of their dipole moments. In the FDTD simulations, this distribution is discretized into a collection of neighboring dipoles separated by a small distance $\Delta y = \Lambda/20$ along the y direction. The radiation output is then computed as the superposition of the light waves emitted by all the dipoles. In the Smith-Purcell geometry of Fig. 1(b), the phase relationship among these dipoles is such that the propagating components of their output fields cancel one another (as expected, since a charge in uniform rectilinear motion does not radiate). The superposition of the evanescent components, however, remains finite, and can be diffracted into radiation by the nearby grating. The end

result is light emission at a discrete set of frequencies associated with the different orders of diffraction. In this framework, the dephasing effect of electronic scattering can also be included by setting the length of the equivalent dipole distribution equal to the electron mean free path between consecutive collisions l_m . As a result, coherent electron-beam radiation is only produced over a finite number of periods equal to l_m/Λ , as in the case of an electron undergoing recurrent collisions in a realistic sample.

Next, we consider a ZZ-GNR or AC-SWNT of length L and electron density N (e.g., introduced via electrostatic doping with a back gate), in the geometry of Fig. 1(a) or 1(b) under a bias voltage V . Its total output power spectrum per unit length can be calculated as follows

$$P_{\text{tot}}(v) = \frac{2}{L} \sum_k P_k(v) f(E_0(k)) [1 - f(E_0(k) - hv)], \quad (7)$$

where v is the emission frequency, the factor of 2 accounts for the spin degeneracy, $E_0(k)$ is the dispersion relation of the lowest conduction subband, $P_k(v)$ is the output power spectrum of a single electron in the Bloch state of energy $E_0(k)$, and f is the electronic distribution function. Pauli blocking effects are explicitly included in this equation through the last two terms, where $f(E_0(k))$ is the probability that the initial electronic state is occupied, and $1 - f(E_0(k) - hv)$ is the probability that the corresponding final state after photon emission is empty. It should be noted that eq. (7) does not include any contribution to the output radiation from the higher-energy subbands of the wire, even though these subbands may contain an appreciable number of electrons (particularly in highly doped and/or large wires). The reason is that (quasi)ballistic transport in these 1D carbon conductors has only been measured in the lowest-energy subbands (i.e., the partially flat subbands involving edge states in ZZ-GNRs [9], and the linear subbands with zero energy separation in metallic SWNTs [2-4]). In contrast, for the higher-energy

subbands the measured mean free paths are too small to allow for appreciable electron-beam radiation.

For each device geometry (either cyclotron-like or Smith-Purcell), the single-electron emission spectra $P_k(v)$ depend on the wavevector k only through the velocity $v_k = dE_0/d(\hbar k)$. These spectra are computed via the FDTD simulations described above for a selection of all possible velocities $v_k \leq v_F$, and are generally found to consist of a sharp peak at a frequency on the order of v_k/Λ (weaker features at higher-order harmonics are also obtained in the same calculations, but are not considered in the following analysis for simplicity). From these simulation results, the center frequency, full width at half maximum (FWHM), and integrated power of each peak are determined. Next, the values of the same parameters for all other velocities v_k are extrapolated using a polynomial fit. The single-electron spectra $P_k(v)$ for all values of v_k are then approximated in eq. (7) with Gaussian peaks having the correct center frequencies, FWHMs, and integrated powers (as determined with this fitting procedure). The choice of a Gaussian function is consistent with the shape of the FDTD single-electron emission peaks, and does not in any case significantly affect the resulting shape of $P_{\text{tot}}(v)$.

Finally, the occupation probabilities f in eq. (7) are computed using a standard model for the electronic distribution function of ballistic conductors with ideal (i.e., reflection-less) contacts [56]. In this model, all electrons moving from left to right can only originate from (and therefore must be in thermal equilibrium with) the contact on the left side of the conductor, and vice versa. As a result, for states with positive velocity (i.e., with $dE_0/dk > 0$), the occupation probability $f(E_0(k))$ can be taken to be a Fermi-Dirac distribution function with Fermi energy equal to the chemical potential μ_l of the left contact. Similarly, all electrons in states with $dE_0/dk < 0$ can be assumed to be in thermal equilibrium with the same chemical potential μ_r .

as the right contact. To determine μ_l and μ_r , first we note that their difference must be equal to the applied voltage V times the electron charge $-q$. Second, we require that the sum of the occupation probabilities of all states in the conducting wire (including states in the higher-energy subbands) must be equal to the electron density N . The same description of the electronic distribution function f leads to the Landauer formulation of conduction, which provides a well-established model of (quasi)ballistic transport [56].

IV. RESULTS AND DISCUSSION

The simulation methods just described were applied to several structures based on the corrugated wire of Fig. 1(a) or the Smith-Purcell configuration of Fig. 1(b), for different values of the period Λ and the electron mean free path l_m . In each structure the substrate material below the conducting wire is SiO₂, modeled with a frequency-dependent permittivity from the internal database of the FDTD simulation engine [54]. This choice of substrate material is based on the aforementioned measurements of (quasi)ballistic transport with metallic SWNTs [2-4]. Alternative substrates may also be considered for the same devices, including hexagonal-BN, SiC (as used with the ballistic ZZ-GNRs of ref. 9), and HfO₂. In fact, theoretical studies indicate that improved transport properties may be obtained with carbon-based conductors deposited or grown on such substrates, due to reduced remote scattering from surface optical phonons and coupled plasmon-phonon modes compared to SiO₂ [57, 58]. The corrugation of the cyclotron-like samples is sinusoidal with amplitude $A = \Lambda/4$, whereas in the Smith-Purcell devices the grating consists of rectangular ridges of width $W = \Lambda/2$ and height $H = 300$ nm. These parameters were selected via initial FDTD simulations so as to maximize the output radiation power. The lateral dimensions of the 1D conductors are the same as in the band-structure

calculations of section II, i.e., the simulated ZZ-GNRs have a width of 40 nm (as in the ballistic samples of ref. 9) and the AC-SWNTs have a typical nanotube diameter of 2 nm. Additional calculations show that the output radiation depends only weakly on these lateral dimensions, as long as the dispersion of the lowest-energy conduction subband maintains the same features shown in Figs. 3 and 4.

In the FDTD calculations of the single-electron emission spectra, the computational domain has the shape of a cube centered about the dipole distribution, with 600- μm side length and perfectly matched layers on all boundaries. The corrugated substrate or grating lies at the center of the x - y plane, with $5 \times 5 \mu\text{m}^2$ area. All the FDTD computational parameters including mesh size and frequency resolution were optimized through extensive convergence tests. In passing, we note that the large disparity between the calculated emission wavelengths (several 10 μm) and the periodicities of the underlying nanostructures (a few 100 nm) makes these simulations extremely demanding in terms of computational resources. As explained above, in the FDTD calculations we consider an electron traveling along the conductor trajectory at a few different velocities v_k (specifically, 0.2, 0.4, 0.6, 0.8, and 1 times the graphene Fermi velocity v_F). The details of the conductor band structure (ZZ-GNR versus AC-SWNT) are then introduced when the total output power spectra are computed from the FDTD simulation results using eq. (7). In all calculations presented below based on this equation we assume a Fermi energy $E_F = 100$ meV above the Dirac point, an applied bias voltage $V = 0.1$ V, and room temperature. In the case of ZZ-GNRs, a wide range of electron velocities $v_k \leq v_F$ contribute to $P_{\text{tot}}(v)$, due to the significant curvature of the lowest-energy conduction subband near such Fermi energy. In AC-SWNTs the lowest-energy conduction subband is relatively linear near E_F and all radiating electrons have velocity close to v_F .

Representative FDTD simulation results for a cyclotron-like device are shown in Fig. 5 for all five electron velocities considered. Specifically, the traces plotted in this figure are obtained by dividing the single-electron power spectra $P_k(\nu)$ by the photon energy $h\nu$, which gives the photon emission rate per unit frequency. The corrugation period Λ here is 68 nm, and the corresponding length l_{cycle} traveled by the electron in each cycle of the sinusoidal trajectory is approximately 100 nm. The mean free path l_m (i.e., the length of the equivalent dipole distribution in the FDTD simulations) is taken to be 3 μm , which is large enough to ensure that the resulting broadening does not affect the shape of the output spectra $P_{tot}(\nu)$, but otherwise reasonably short to minimize the computational time. The results presented here therefore apply to the optimal case of highly ballistic samples, whereas the effect of shorter mean free paths is described later in this section. For each electron velocity v_k , the frequency of peak emission in the spectra of Fig. 5 is approximately equal to v_k/l_{cycle} (i.e., $v_k/v_F \times 10$ THz for $l_{cycle} = 100$ nm), which is consistent with expectations for cyclotron-like radiation [55]. It should be noted that only a relatively narrow spectral region is considered in each one of these calculations, centered about the main radiation peak, so that the aforementioned weaker emission features at higher-order harmonics are not included.

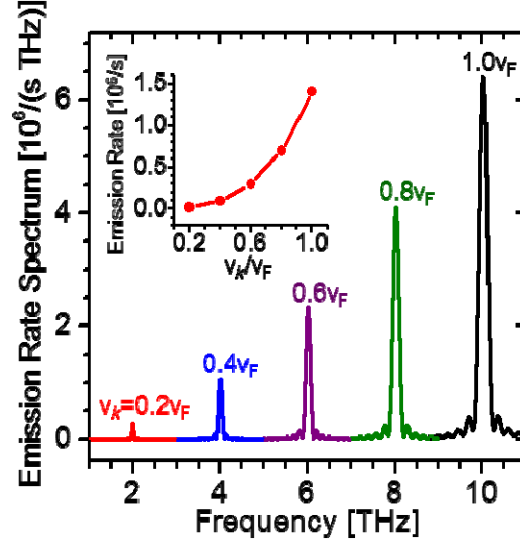


FIG. 5: Photon emission rate per unit frequency of an electron in a corrugated carbon nanowire, plotted as a function of radiated frequency for five different values of the electron velocity v_k . The corrugation period and amplitude are 68 nm and 17 nm, respectively. Inset: total photon emission rate of the same electron, integrated over all frequencies, versus electron velocity.

The spectra of Fig. 5 also show that the single-electron output power increases rapidly with increasing electron speed. This behavior is again in agreement with basic expectations: for example, according to the Larmor formula for cyclotron radiation (which however only applies in the limit of $A \ll \lambda$) [55]. Therefore the radiation mechanisms under study benefit strongly from the relatively large electron velocities of carbon-based nanostructures. In particular, in the AC-SWNTs of Fig. 4, the slope of the lowest-energy conduction and valence subbands is approximately equal to $\approx 1 \times 10^8$ cm/s over a broad energy range across the Dirac point. In the ZZ-GNRs of Fig. 3, the lowest subbands feature a nearly flat dispersion with almost zero velocity near the Dirac point, but their slope then rapidly approaches as the energy is increased or decreased beyond a few ± 10 meV. As already mentioned, in the calculations presented below we assume a chemical potential $E_F = 100$ meV,

so that even in the ZZ-GNRs the carriers near the Fermi level [i.e., the carriers that produce the largest contribution to the sum of eq. (7)] travel at a relatively high velocity close to v_F .

The inset of Fig. 5 shows the total emission rate $1/\tau_{rad}$ integrated over all frequencies and plotted as a function of electron velocity. Values above 1×10^6 photons/s are obtained for $v_k \approx v_F$, corresponding to a radiative lifetime τ_{rad} of less than 1 μ s. We emphasize that such emission rates are significant at THz frequencies. In fact, similar or smaller rates are obtained for spontaneous emission from the active materials of THz quantum cascade lasers (QCLs), which represent the current state-of-the-art for solid-state THz sources, albeit limited to operation at cryogenic temperatures [23]. For example, spontaneous emission lifetimes ranging from 3 μ s to over 60 μ s are reported in refs. 59-61 for different THz QCL designs. Finally, we note that the same FDTD simulations of Fig. 5 applied to Smith-Purcell devices produce qualitatively similar results.

Figure 6 shows a selection of emission spectra $P_{tot}(v)$ computed with eq. (7) for different combinations of carbon nanostructure (ZZ-GNR or AC-SWNT) and radiation mechanism (cyclotron-like or Smith-Purcell). Each panel contains four spectra corresponding to different values of the corrugation or grating period Λ . These values were selected to produce emission peaked near 4, 6, 8, and 10 THz, as an illustration of the inherent geometric tunability of the underlying radiation mechanisms. The linewidth and shape of these spectra are determined almost entirely by the dispersion of the single-electron emission frequency with velocity $|v_k|$. In general, the output radiation is mostly produced by the electrons in states within a few units of thermal energy $k_B T$ from the Fermi level, due to Pauli blocking constraints. The emission spectra then depend on the velocity distribution of these electrons, which can be inferred from Figs. 3 and 4. In ZZ-GNR samples, $|v_k|$ near E_F exhibits an appreciable variation with k , which

results in the asymmetric broadening observed in Figs. 6(a) and 6(b), with the slower electrons emitting at lower frequencies and at a smaller rate. In AC-SWNTs, γ near E_F is nearly constant with k , but with slightly different values in the two branches of opposite slope on either side of each conduction-subband minimum. As a result, the AC-SWNT emission spectra consist of two narrow overlapping peaks centered at slightly different frequencies, which can be observed most clearly in the 10-THz feature of Fig. 6(c). In any case, all spectra shown in Fig. 6 are significantly narrower than the output of similar radiation mechanisms in 2D graphene samples [45, 46], which suffer from substantial broadening caused by carriers traveling along different directions and emitting at different frequencies.

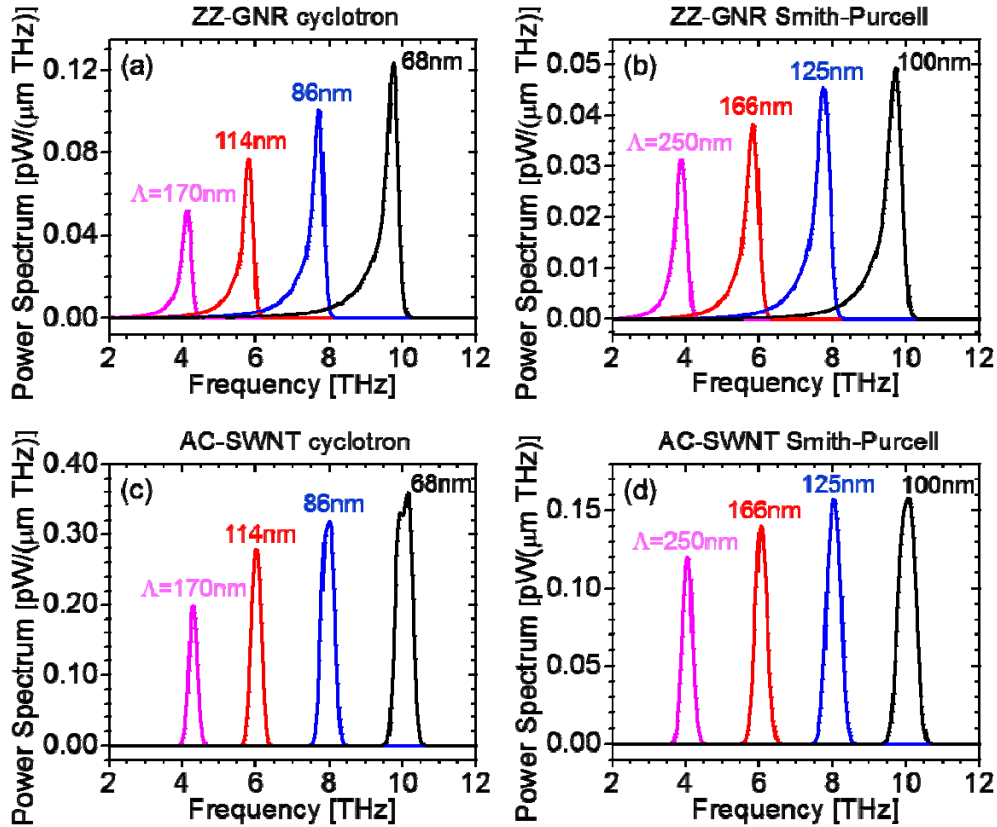


FIG. 6: Output radiation spectra per unit length for different periods of the grating or corrugation: (a) cyclotron-like radiation from sinusoidally corrugated ZZ-GNRs; (b) Smith-Purcell emission from ZZ-GNRs near a rectangular grating; (c) cyclotron-like radiation from sinusoidally corrugated AC-SWNTs; (d) Smith-Purcell emission from AC-SWNTs near a rectangular grating.

The total radiation power per unit length produced by the structures of Fig. 6, integrated over all frequencies, is plotted as a function of the corresponding frequency of peak emission in Fig. 7. The comparison among the different nanomaterials and radiation mechanisms under study is clearly displayed in this figure. For both types of 1D conductors (ZZ-GNRs and AC-SWNTs), cyclotron-like emission is always more efficient than Smith-Purcell radiation. This observation makes intuitive sense, since the latter mechanism involves charges in uniform rectilinear motion and relies on the (non-unity) diffraction efficiency of the underlying grating. Furthermore, regardless of the emission process, AC-SWNTs consistently produce stronger radiation than ZZ-GNRs emitting at the same frequency. This difference can be ascribed to the more favorable band structure of metallic nanotubes, which leads to a narrower distribution of carrier velocities near the maximum speed for all the radiating charges.

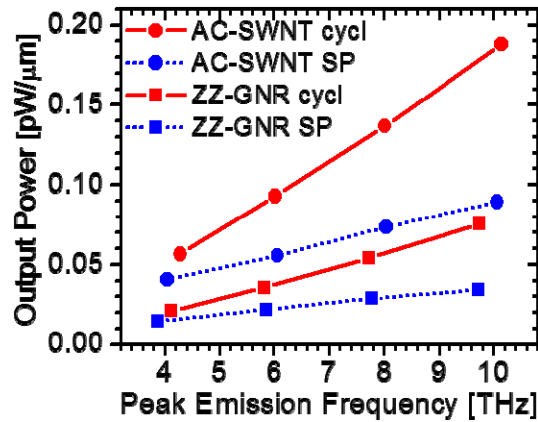


FIG. 7: Total output power per unit length of the structures of Fig. 6, integrated over all frequencies and plotted as a function of the corresponding frequency of peak emission.

The data of Fig. 7 also show that experimentally measurable cyclotron-like or Smith-Purcell radiation can be produced even by a single nanotube or nanoribbon. Specifically, for all structures considered in this figure, output powers of several pW (i.e., above the noise equivalent power of standard Si THz bolometers) are obtained with reasonable conductor lengths of about

100 μm . For comparison, we also note that the power levels per unit length shown in Fig. 7 are three orders of magnitude higher than theoretical predictions for THz interband spontaneous emission across fully inverted bands in metallic SWNTs [38]. The device structures under study can therefore be envisioned as promising building blocks for future nanoscale electronic circuits operating at ultrahigh frequencies. Furthermore, if the same structures can be integrated in high-density arrays, technologically significant power levels for THz-photonics applications are obtained (e.g., in the μW range). In particular, the ballistic ZZ-GNRs described in section II.A are produced by epitaxial growth techniques [9], which are readily applicable to the fabrication of ordered arrays with macroscale (e.g., mm-range) dimensions. Significant progress has also been reported in recent years towards the synthesis of high-density arrays of aligned nanotubes [44, 62]. In principle, these ZZ-GNR or AC-SWNT arrays could also be combined with an optical cavity for the demonstration of coherent stimulated emission, and ultimately even lasing, in analogy with the operation of traditional FELs. The design and analysis of suitable device geometries will be the subject of future study.

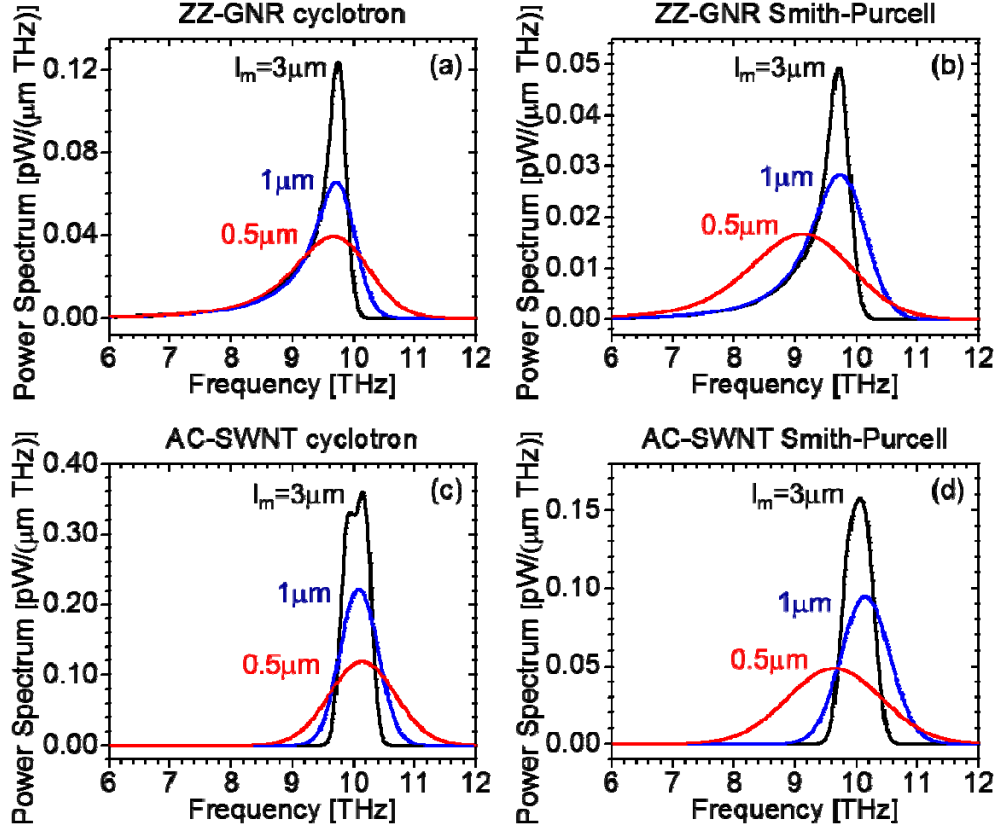


FIG. 8: Output radiation spectra per unit length for different values of the electronic mean free path: (a) cyclotron-like radiation from sinusoidally corrugated ZZ-GNRs; (b) Smith-Purcell emission from ZZ-GNRs near a rectangular grating; (c) cyclotron-like radiation from sinusoidally corrugated AC-SWNTs; (d) Smith-Purcell emission from AC-SWNTs near a rectangular grating.

Finally, the effect of electronic collisions is illustrated in Fig. 8, where again each panel corresponds to a different combination of carbon nanostructure and radiation mechanism. In each case, we consider three different values of the mean free path l_m (i.e., the length of the equivalent dipole distribution in the FDTD simulations), namely 3, 1, and 0.5 μm . The period Λ is fixed at the value that produces emission near 10 THz (68 and 100 nm for the cyclotron-like and Smith-Purcell devices, respectively), and all other parameters are the same as in Fig. 6. As expected, decreasing the electronic mean free path causes a broadening of the emission spectra and a reduction in their peak values. A shift in the center frequencies is also observed

(particularly in the case of Smith-Purcell emission), as is often the case in the presence of collision broadening [63]. In any case, even for the lowest mean free path of $0.5\text{ }\mu\text{m}$ considered in these plots, the emission peaks remain well resolved with relatively large quality factor. The key conclusion is that the radiation phenomena under study can be implemented using realistic high-quality samples based on existing technologies.

V. CONCLUSIONS

In summary, we have investigated numerically the use of 1D carbon nanostructures (specifically ZZ-GNRs and AC-SWNTs) for the generation of THz light based on two related electron-beam radiation mechanisms (i.e., cyclotron-like emission in the presence of mechanical corrugation and the Smith-Purcell effect). In all cases we find that experimentally accessible output powers at geometrically tunable THz frequencies can be obtained even with individual nanowires. Of all combinations of radiation mechanism and carbon nanostructure considered, cyclotron-like emission from AC-SWNTs produces the highest output power at all frequencies. On the other hand, ZZ-GNRs have the advantage of more immediate compatibility with integration in high-density arrays, at least based on current fabrication methods. The cyclotron-like sample geometry may also be more challenging to implement compared to Smith-Purcell devices, due to the critical requirement of conformal adhesion on a nanoscale sinusoidal grating. Both radiation mechanisms are also found to be relatively robust with respect to electronic collisions, with pronounced emission peaks obtained even in the presence of sub-micron mean free paths. These results suggest that 1D carbon nanostructures represent a uniquely suited materials platform for the demonstration and study of electron-beam radiation processes in condensed matter. Possible applications include ultrahigh-frequency oscillators for future nanoelectronic circuits, and (in the

case of high-density arrays) radiation sources for THz photonics. The observed increase in output power with increasing frequency of peak emission (see Fig. 7) is particularly significant in this respect, since existing room-temperature THz sources are limited to frequencies below ~ 1 THz [23]. The radiation mechanisms under study may therefore provide a promising solution to this important technology gap.

Acknowledgments: This work was supported by the National Science Foundations under Grant #DMR-1308659. The FDTD simulations were performed using the Shared Computing Cluster facility at Boston University.

References:

1. S. Frank, P. Poncharal, Z. L. Wang, and W. A. de Heer, “Carbon nanotube quantum resistors,” *Science* **280**, 1744-1746 (1998).
2. A. Javey, J. Guo, M. Paulsson, Q. Wang, D. Mann, M. Lundstrom, and H. Dai, “High-field quasiballistic transport in short carbon nanotubes,” *Phys. Rev. Lett.* **92**, 106804 (2004).
3. J.-Y. Park, S. Rosenblatt, Y. Yaish, V. Sazonova, H. Üstünel, S. Braig, T. A. Arias, P. W. Brouwer, and P. L. McEuen, “Electron-phonon scattering in metallic single-walled carbon nanotubes,” *Nano Lett.* **4**, 517–520 (2004).
4. M. S. Purewal, B. H. Hong, A. Ravi, B. Chandra, J. Hone, and P. Kim, “Scaling of resistance and electron mean free path of single-walled carbon nanotubes,” *Phys. Rev. Lett.* **98**, 186808 (2007).
5. K. I. Bolotin, K. J. Sikes, J. Hone, H. L. Stormer, and P. Kim, “Temperature-dependent transport in suspended graphene,” *Phys. Rev. Lett.* **101**, 096802 (2008).
6. X. Du, I. Skachko, A. Barker, and E. Y. Andrei, “Approaching ballistic transport in suspended graphene,” *Nature Nanotechnol.* **3**, 491-495 (2008).
7. A. S. Mayorov, R. V. Gorbachev, S. V. Morozov, L. Britnell, R. Jalil, L. A. Ponomarenko, P. Blake, K. S. Novoselov, K. Watanabe, T. Taniguchi, and A. K. Geim, “Micrometer-scale ballistic transport in encapsulated graphene at room temperature,” *Nano Lett.* **11**, 2396-2399 (2011).
8. L. Wang, I. Meric, P. Y. Huang, Q. Gao, Y. Gao, H. Tran, T. Taniguchi, K. Watanabe, L. M. Campos, D. A. Muller, J. Guo, P. Kim, J. Hone, K. L. Shepard, and C. R. Dean, “One-dimensional electrical contact to a two-dimensional material,” *Science* **342**, 614-617 (2013).

9. J. Baringhaus, M. Ruan, F. Edler, A. Tejeda, M. Sicot, A. Taleb-Ibrahimi, A.-P. Li, Z. Jiang, E. H. Conrad, C. Berger, C. Tegenkamp, and W. A. de Heer, “Exceptional ballistic transport in epitaxial graphene nanoribbons,” *Nature* **506**, 349-354 (2014).
10. S. J. Smith and E. M. Purcell, “Visible light from localized surface charges moving across a grating,” *Phys. Rev.* **92**, 1069 (1953).
11. T. C. Marshall, *Free Electron Lasers* (Macmillan, 1985).
12. V. L. Bratman, B. S. Dumesht, A. E. Fedotov, P. B. Makhlov, B. Z. Movshevich, and F. S. Rusin, “Terahertz orotrons and oromultipliers,” *IEEE Trans. Plasma Sci.* **38**, 1466-1471 (2010).
13. C. Wirner, C. Kiener, W. Boxleitner, M. Witzany, E. Gornik, P. Vogl, G. Böhm, and G. Weimann, “Direct observation of the hot electron distribution function in GaAs/AlGaAs heterostructures,” *Phys. Rev. Lett.* **70**, 2609-2612 (1993).
14. S. A. Mikhailov, “Plasma instability and amplification of electromagnetic waves in low-dimensional electron systems,” *Phys. Rev. B* **58**, 1517-1532 (1998).
15. A. I. Fedorchenko, H. H. Cheng, G. Sun, and R. A. Soref, “Radiation emission from wrinkled SiGe/SiGe nanostructures,” *Appl. Phys. Lett.* **96**, 113104 (2010).
16. D. D. Smith and A. Belyanin, “Room-temperature semiconductor coherent Smith–Purcell terahertz sources,” *Appl. Phys. Lett.* **98**, 063501 (2011).
17. P. M. van den Berg, “Smith-Purcell radiation from a point charge moving parallel to a reflection grating,” *J. Opt. Soc. Am.* **63**, 1588-1597 (1973).
18. Interestingly, reference 14 also predicts that coherent emission and amplification near the Smith-Purcell frequency v_d/Λ can be obtained in the classical drift transport regime, in the

limit of high drift velocity v_d and/or low carrier density N . However, the required conditions on v_d and N are not satisfied in typical grating-coupled semiconductor 2DEGs.

19. D. C. Tsui, E. Gornik, and R. A. Logan, “Far infrared emission from plasma oscillations of Si inversion layers,” *Solid State Commun.* **35**, 875-877 (1980).
20. R. A. Höpfel, E. Vass, and E. Gornik, “Thermal excitation of two-dimensional plasma oscillations,” *Phys. Rev. Lett.* **49**, 1667-1671 (1982).
21. N. Okisu, Y. Sambe, and T. Kobayashi, “Far-infrared emission from two-dimensional plasmons in AlGaAs/GaAs heterointerfaces,” *Appl. Phys. Lett.* **48**, 776-778 (1986).
22. K. Hirakawa, K. Yamanaka, M. Grayson, and D. C. Tsui, “Far-infrared emission spectroscopy of hot two-dimensional plasmons in $\text{Al}_{0.3}\text{Ga}_{0.7}\text{As}/\text{GaAs}$ heterojunctions,” *Appl. Phys. Lett.* **67**, 2326-2328 (1995).
23. M. Lee and M. C. Wanke, “Searching for a solid-state terahertz technology,” *Science* **316**, 64-65 (2007).
24. T. Low and P. Avouris, “Graphene plasmonics for terahertz to mid-infrared applications,” *ACS Nano* **8**, 1086–1101 (2014).
25. A. Tredicucci and M. S. Vitiello, “Device concepts for graphene-based terahertz photonics,” *IEEE J. Select. Topics Quantum Electron.* **20**, 8500109 (2014).
26. R. R. Hartmann, J. Kono, and M. E. Portnoi, “Terahertz science and technology of carbon nanomaterials,” *Nanotechnology* **25**, 322001 (2014).
27. V. Ryzhii, M. Ryzhii, and T. Otsuji, “Negative dynamic conductivity of graphene with optical pumping,” *J. Appl. Phys.* **101**, 083114 (2007).
28. F. Rana, “Graphene terahertz plasmon oscillators,” *IEEE Trans. Nanotechnol.* **7**, 91-99 (2008).

29. V. Ryzhii, M. Ryzhii, V. Mitin, and M. S. Shur, “Graphene tunneling transit-time terahertz oscillator based on electrically induced p–i–n junction,” *Appl. Phys. Express* **2**, 034503 (2009).
30. V. Ryzhii, M. Ryzhii, V. Mitin, and T. Otsuji, “Toward the creation of terahertz graphene injection laser,” *J. Appl. Phys.* **110**, 094503 (2011).
31. S. A. Mikhailov, “Graphene-based voltage-tunable coherent terahertz emitter,” *Phys. Rev. B* **87**, 115405 (2013).
32. B. Sensale-Rodriguez, “Graphene-insulator-graphene active plasmonic terahertz devices,” *Appl. Phys. Lett.* **103**, 123109 (2013).
33. A. S. Moskalenko and S. A. Mikhailov, “Radiative damping and synchronization in a graphene-based terahertz emitter,” *J. Appl. Phys.* **115**, 203110 (2014).
34. A. S. Maksimenko and G. Ya. Slepyan, “Negative differential conductivity in carbon nanotubes,” *Phys. Rev. Lett.* **84**, 362 (2000).
35. D. Dragoman and M. Dragoman, “Terahertz oscillations in semiconducting carbon nanotube resonant-tunneling diodes,” *Physica E* **24**, 282-289 (2004).
36. O. V. Kibis, D. G. W. Parfitt, and M. E. Portnoi, “Superlattice properties of carbon nanotubes in a transverse electric field,” *Phys. Rev. B* **71**, 035411 (2005).
37. A. M. Nemilentsau, G. Ya. Slepyan, and S. A. Maksimenko, “Thermal radiation from carbon nanotubes in the terahertz range,” *Phys. Rev. Lett.* **99**, 147403 (2007).
38. O. V. Kibis, M. Rosenau da Costa, and M. E. Portnoi, “Generation of terahertz radiation by hot electrons in carbon nanotubes,” *Nano Lett.* **7**, 3414–3417 (2007).
39. M. E. Portnoi, O. V. Kibis, M. Rosenau da Costa, “Terahertz applications of carbon nanotubes,” *Superlattices Microstruct.* **43**, 399–407 (2008).

40. D. Sun, C. Divin, J. Rioux, J. E. Sipe, C. Berger, W. A. de Heer, P. N. First, and T. B. Norris, “Coherent control of ballistic photocurrents in multilayer epitaxial graphene using quantum interference,” *Nano Lett.* **10**, 1293-1296 (2010).
41. S. Boubanga-Tombet, S. Chan, T. Watanabe, A. Satou, V. Ryzhii, and T. Otsuji, “Ultrafast carrier dynamics and terahertz emission in optically pumped graphene at room temperature,” *Phys. Rev. B* **85**, 035443 (2012).
42. L. Pechtel, L. Song, D. Schuh, P. Ajayan, W. Wegscheider, and A. W. Holleitner, “Time-resolved ultrafast photocurrents and terahertz generation in freely suspended graphene,” *Nature Comm.* **3**, 646 (2012).
43. Y.-M. Bahk, G. Ramakrishnan, J. Choi, H. Song, G. Choi, Y. H. Kim, K. J. Ahn, D.-S. Kim, and P. C. M. Planken, “Plasmon enhanced terahertz emission from single layer graphene,” *ACS Nano* **8**, 9089–9096 (2014).
44. L. V. Titova, C. L. Pint, Q. Zhang, R. H. Hauge, J. Kono, and F. A. Hegmann, “Generation of terahertz radiation by optical excitation of aligned carbon nanotubes,” *Nano Lett.* **15**, 3267–3272 (2015).
45. K. Tantiwanichapan, J. DiMaria, S. N. Melo, and R. Paiella, “Graphene electronics for terahertz electron-beam radiation,” *Nanotechnology* **24**, 375205 (2013).
46. K. Tantiwanichapan, X. Wang, A. K. Swan, and R. Paiella, “Graphene on nanoscale gratings for the generation of terahertz Smith-Purcell radiation,” *Appl. Phys. Lett.* **105**, 241102 (2014).
47. K. Nakada, M. Fujita, G. Dresselhaus, and M. S. Dresselhaus, “Edge state in graphene ribbons: nanometer size effect and edge shape dependence,” *Phys. Rev. B* **54**, 17954 (1996).

48. M. I. Katsnelson, *Graphene: Carbon in Two-Dimensions* (Cambridge University Press, 2012).
49. J. J. Palacios, J. Fernández-Rossier, L. Brey and H. A. Fertig, “Electronic and magnetic structure of graphene nanoribbons,” *Semicond. Sci. Technol.* **25**, 033003 (2010).
50. L. Yang, C.-H. Park, Y.-W. Son, M. L. Cohen, and S. G. Louie, “Quasiparticle energies and band gaps in graphene nanoribbons,” *Phys. Rev. Lett.* **99**, 186801 (2007).
51. K. Wakabayashi, Y. Takane, and M. Sigrist, “Perfectly conducting channel and universality crossover in disordered graphene nanoribbons,” *Phys. Rev. Lett.* **99**, 036601 (2007).
52. R. Saito, G. Dresselhaus, and M. S. Dresselhaus, *Physical Properties of Carbon Nanotubes* (Imperial College Press, 1998).
53. C. T. White and T. N. Todorov, “Carbon nanotubes as long ballistic conductors,” *Nature* **393**, 240-242 (1998).
54. FDTD Solutions, version 8.12 (Lumerical Solutions, Vancouver, 2015).
55. J. D. Jackson, *Classical Electrodynamics* (Wiley, 1975).
56. S. Datta, *Electronic Transport in Mesoscopic Systems* (Cambridge University Press, 1995).
57. S. Fratini and F. Guinea, “Substrate-limited electron dynamics in graphene,” *Phys. Rev. B* **77**, 195415 (2008).
58. Z.-Y. Ong and M. V. Fischetti, “Theory of interfacial plasmon-phonon scattering in supported graphene,” *Phys. Rev. B* **86**, 165422 (2012).
59. B. Xu, Q. Hu, and M. R. Melloch, “Electrically pumped tunable terahertz emitter based on intersubband transition,” *Appl. Phys. Lett.* **71**, 440-442 (1997).

60. M. Rochat, J. Faist, M. Beck, U. Oesterle, and M. Illegems, “Far-infrared ($\lambda = 88 \mu\text{m}$) electroluminescence in a quantum cascade structure,” *Appl. Phys. Lett.* **73**, 3724-3726 (1998).
61. B. S. Williams, B. Xu, Q. Hu, and M. R. Melloch, “Narrow-linewidth terahertz intersubband emission from three-level systems,” *Appl. Phys. Lett.* **75**, 2927-2929 (1999).
62. S. J. Kang, C. Kocabas, T. Ozel, M. Shim, N. Pimparkar, M. A. Alam, S. V. Rotkin, and J. A. Rogers, “High-performance electronics using dense, perfectly aligned arrays of single-walled carbon nanotubes,” *Nature Nanotechnol.* **2**, 230-236 (2007).
63. G. Peach, “Theory of the pressure broadening and shift of spectral lines,” *Adv. Phys.* **30**, 367-474 (1981).